Boosting CO_2 Photoreduction by π-π-Induced Preassembly between a Cu(I) Sensitizer and a Pyrene-Appended Co(II) Catalyst

Jia-Wei Wang,[1,2] Zizi Li,[1] Zhi-Mei Luo,[2] Yanjun Huang,[1] Fan Ma,[1] Stephan Kupfer,*[3] Gangfeng Ouyang*[1,4,5]*

[1]KLGHEI of Environment and Energy Chemistry, School of Chemistry, Sun Yat-sen University, Guangzhou, 510275, China

[2]Institute of Chemical Research of Catalonia (ICIQ), Barcelona Institute of Science and Technology (BIST), Avinguda Paisos Catalans 16, Tarragona 43007, Spain.

[3]Institute of Physical Chemistry, Friedrich Schiller University Jena, Helmholtzweg 4, Jena 07743, Germany

[4]Chemistry College, Center of Advanced Analysis and Gene Sequencing, Zhengzhou University, Zhengzhou 450001, China

[5]Guangdong Provincial Key Laboratory of Emergency Test for Dangerous Chemicals, Guangdong Institute of Analysis (China National Analytical Center Guangzhou), Guangzhou, 510070, China

Correspondence and requests for materials should be addressed to J.-W.W (wangjw25@mail2.sysu.edu.cn), S.K. (stephan.kupfer@uni-jena.de) and O.G. (cesoygf@mail.sysu.edu.cn)

ABSTRACT: The design of a highly efficient system for CO_2 photoreduction fully based on earth-abundant elements presents a challenge, which may be overcome by installing suitable interactions between photosensitizer and catalyst to expedite the intermolecular electron transfer. Herein we have designed a pyrene-decorated Cu(I) complex with a rare dual-emission behavior, aiming at additional π-interaction with a pyrene-appended Co(II) catalyst for visible-light-driven CO_2-to-CO conversion. The results of ^{1}H NMR titration, time-resolved fluorescence/absorption spectroscopies, quantum chemical simulations and photocatalytic experiments clearly demonstrate that the dynamic π-π interaction between sensitizer and catalyst is highly advantageous in photocatalysis by accelerating the intermolecular electron transfer rate up to 6.9×10^5 s^{-1}, thus achieving a notable apparent quantum yield of 19% at 425 nm with near-unity selectivity. While comparable to most earth-abundant molecular systems, this value is over three-times of the pyrene-free system (6.0%) and far surpassing the benchmarking Ru(II) tris(bipyridine) (0.3%) and Ir(III) tris(2-phenylpyridine) (1.4%) photosensitizers under parallel conditions.

Significance statement: The sunlight-driven reduction of CO_2 into products like CO, CH_4, etc. can lower the atmospheric CO_2 concentration and provide carbon-neutral energy simultaneously, attracting scientists to design photocatalytic systems to facilitate this process. The rational construction of non-covalent interactions between photosensitizers and catalysts may serve as a versatile strategy to boost catalytic efficiency by speeding up the electron transfer. Besides performance, it is also desirable to lower the expense by developing photocatalytic systems based on earth-abundant elements instead of precious metals. Herein, for the first time, we present the proof of concept into a fully earth-abundant system by installing dynamic π-π interaction between a dual-emissive, pyrene-decorated Cu(I) photosensitizer and a pyrene-appended Co(II) catalyst, achieving remarkable catalytic performance for visible-light-driven CO_2 reduction.

Competing Interest Statement: We declare no conflict of interest.
Classification: CO_2 reduction
Keywords: noble-metal-free system • photocatalytic CO_2 reduction • molecular catalysis • electron transfer • *π-π* interaction

Introduction

Reductive transformation of CO_2 powered by solar energy to produce renewable fuels is auspicious to relieve energy shortage and achieve carbon neutrality (1, 2). The rational design of catalytic systems is the key to accelerating the light-driven CO_2 reduction since this reaction suffers from sluggish multi-electron reaction kinetics and strong competition with proton reduction (3, 4). Metal complexes as molecular photosensitizers (PSs) and/or catalysts can serve as essential components in the photocatalytic system, which can be optimized with mechanistic investigations and synthetic modifications on their well-defined structures (5, 6). Ru, Ir and Re complexes have been vastly utilized as potent PSs in CO_2 photoreduction (7, 8), whereas the scarcity of these noble metals restricts their practical uses (9). In this context, earth-abundant molecular systems with organic (10) or metal-organic chromophores with Zn(II) (11), Cu(I) (12) or Al(III) (13) centers have received considerable interest, among which Cu(I)-based PSs are particularly appealing alternatives with their long-lived metal-to-ligand excited states and highly variable luminescent properties with a vast ligand library (14-17). The first report of a Cu(I) PS for CO_2 photoreduction by Ishitani *et al.* (18) displays the design of a diphosphine-dangled phenanthroline ligand to form a dimeric Cu(I) PS. The tetradentate ligand inhibits the decomplexation of the diphosphine donors around the Cu cores, enabling prominent stability during visible-light-driven CO_2 reduction with Fe (18, 19) or Mn (20)

catalysts. Beller *et al.* also developed the use of Cu(I) PSs for CO_2 reduction, in synergy with Fe-cyclopentadienone (21) or Mn-diamine complexes (22) as the catalysts, respectively. Another breakthrough is from Sakai *et al.* (12, 23, 24), in which a water-soluble, a sulphonated Cu(I) PS was designed for CO_2 photoreduction to CO with several derivatives of Co porphyrins, giving good selectivity (ca. 90%) in fully aqueous conditions which often induce significant proton reduction.

Despite the above progress, the performances of the Cu(I)-sensitized systems for CO_2 reduction are still unparallel to those noble-metal-based systems; in turn the effective knowledge-driven concepts to further improve their efficiencies are highly desirable. On one hand, rigorous strategies to tailor ligand functionalities are fundamental to improve the photophysical and photo-redox properties of Cu(I) PSs in photocatalysis. The discovery of novel Cu(I) complexes in terms of coordination structures (25) or emission behaviors (26) may promote the efficiency of CO_2 photoreduction. On the other hand, further improvement can be achieved by the construction of additional interaction between PS and catalyst to expedite the electron transfer and thus curb the self-deactivation of excited PS (27), eventually promoting photocatalysis. This tactic has been applied in the noble-metal-based systems with covalent linking (28-30), H-bonding (31), coordinative connection (32) and π-π interactions (33, 34). Among them, non-covalent π-π interactions are advantageous for providing dynamic interactions rather than stable connections between PS and catalyst, in which the 'dynamic interactions' can be realized by weak and/or reversible intermolecular attractions, allowing both connection and dissociation in a dynamic manner during the photocatalysis. While accelerating the intermolecular electron transfer, the dynamic interactions can concurrently circumvent the irreversible dissociation between the PS and the catalyst with their affinity to regain the association, which is hardly applicable with the linkages based on covalent bonds like C-C, C-N, etc. (32).

With the above anticipated merits, we have designed a noble-metal-free system with π-π interaction between PS and catalyst, by employing a Cu(I) PS with two pyrenyl groups, [Cu^{I}(**xantphos**)(**pybcp**)]PF_6 (**CuPYBCP**; **xantphos** = 9,9-dimethyl-4,5-bis(diphenylphosphino)xanthene, **pybcp** = 2,9-dimethyl-4,7-bis(4-(pyren-1-yl)phenyl)-1,10-phenanthroline) and a Co(II) catalyst, [Co^{II}(**PYN5**)]$(ClO_4)_2$, (**CoPYN5**; **PYN5** = (2*E*,12*E*)-2,13-dimethyl-14-(pyren-1-yl)-3,6,9,12-tetraaza-1(2,6)-pyridinacyclotridecaphane-2,12-diene), respectively. The prototypical PS and catalyst were also employed for comparison, *i.e.*, [Cu^{I}(**xantphos**)(**bcp**)]PF_6 (**CuBCP**; **bcp** = bathocuproine or 2,9-dimethyl-1,10-phenanthroline) and [Co^{II}(**N5**)]$(ClO_4)_2$ (**CoN5**; **N5** = (2*E*,12*E*)-2,13-dimethyl-3,6,9,12-tetraaza-1(2,6)-pyridinacyclotri-decaph-ane-2,12-diene), respectively. Interestingly, the pyrene decoration in **CuPYBCP** endows an unusual dual emission behavior and a sharply decreased lifetime, which has been studied systematically by means of spectroscopic and quantum chemical methods. More importantly, the π-π interaction between **CuPYBCP** and **CoPYN5** has been confirmed to substantially accelerate the electron transfer and improve the photocatalytic performance in CO_2 reduction. Compared to the pyrene-free **CuBCP**/**CoN5** system (6.0%), the π-π interacted **CuPYBCP**/**CoPYN5** system accomplishes a remarkable apparent quantum yield (Φ) of 19% at 425 nm for the CO_2-to-CO conversion with a maximum selectivity of 97%, also surpassing the parallel performances of benchmarking noble-metal PSs. To our knowledge, this is the first example of noble-metal-free molecular system for photocatalytic CO_2 reduction assisted by non-covalent interactions, also presenting a rare case of dual-emissive Cu(I) luminescent complex.

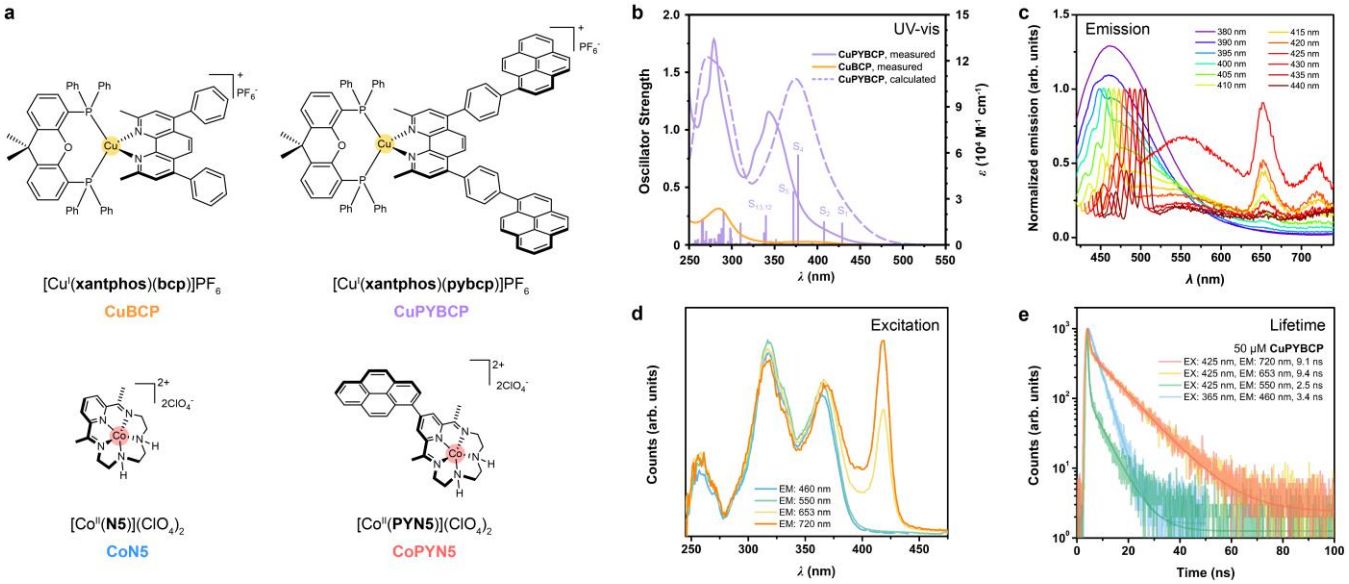

Figure 1. Structures and photophysics. (a) Chemical structures of the used Cu(I) PSs and Co(II) catalysts. (b) UV-vis absorption spectra of 12 μM **CuPYBCP** (violet, solid line) or **CuBCP** (orange, solid line) in CH_3CN. The TDDFT-calculated results of **CuPYBCP** (violet, dashed and dropped lines) are also shown for comparison. (c) Emission spectra of 50 μM **CuPYBCP** upon excitation at 380~440 nm in deaerated CH_3CN. The emission intensity was normalized to the highest Raman peak of CH_3CN. (d) Excitation spectra and (e) excited-state decay traces of 50 μM **CuPYBCP** for different emission bands in deaerated CH_3CN.

Table 1. Summary of the photophysical and redox properties of the Cu(I) PSs.[a]

Cu PS	λ_{ab} (nm)λ_{ab}	λ_{em} (nm)	τ (ns)	Isosbestic point (nm)	$E_{0\text{-}0}$ (V)	E_{red}[d] (V)	E_{ox}[e] (V)	$E_{q,red}$ (V)	$E_{q,ox}$ (V)
CuBCP	320, 388	580[b]	289.0[b]	445	2.79	-1.40	1.52	1.39	-1.27
CuPYBCP	240,279,344	460[b],550[c],653[c],720[c]	3.5 (460 nm)[b] 2.5 (550 nm)[c] 9.4 (653 nm)[c] 9.1 (720 nm)[c]	400	3.10	-1.37	1.59	1.73	-1.51

[a] Measured in deaerated CH_3CN solution at 293 K. Potentials are footnoted vs. NHE. [b] Excitation wavelength is 365 nm. [c] Excitation wavelength is 425 nm. [d] Half-wave potentials ($E_{1/2}$) of reduction waves. [e] Peak potentials of oxidation waves.

Photophysics

The new heteroleptic Cu(I) complex, **CuPYBCP**, in the type $[Cu(P\text{^}P)(N\text{^}N)]^+$, was prepared with the pyrene-appended N^N ligand, **pybcp**, which was synthesized via Suzuki coupling (see Experimental details in SI). The chemical compositions and structures of **pybcp** and **CuPYBCP** were examined by multiple NMR spectroscopies and high-resolution mass spectroscopy (Figure S1-S7).

The UV-vis absorption and steady-state fluorescent spectra of **CuBCP** and **CuPYBCP** in CH_3CN show significant differences (Figure 1b). The UV-vis spectrum of **CuBCP** displays the characteristic ligand-centered and MLCT bands at 285 and 388 nm (35), respectively. In sharp contrast, several bands appear on the absorption spectra of **CuPYBCP** with much stronger absorption coefficient values, manifesting the significant hyperchromic effect of pyrenyl groups for a stronger visible-light absorption ability. Quantum chemical simulations performed at the time-dependent density functional level of theory (TDDFT; Table S1 and S2) were carried out in order to unambiguously unravel the nature of the electronic transitions underlying the absorption bands of **CuPYBCP**; fully relaxed structures for all calculated intermediates are collected (36). TDDFT predicts two dipole-allowed $MLCT_{phen}$ excitations, i.e., into the S_1 and S_2 singlet excited states at 429 and 408 nm from Cu to the lowest two π^*_{phen} orbitals of the phenanthroline moiety – associated with the red-sided shoulder at approximately 400 nm (Figure 1b). According to the simulations, the prominent absorption feature – arising upon incorporation of the pyrene motifs in PS – measured at 344 nm originates from two strongly dipole-allowed intra-ligand charge transfer (ILCT; S_4 and S_5) transitions at 377 and 372 nm. These transitions involve shifts in electronic density from the π_{pyr} orbitals of each pyrene group into the lowest energy π^*_{phen} orbital. Further, S_{12} and S_{13} (340 and 338 nm) featuring a mixed electronic character involving local excitations of the pyrenes as well as charge transfer from the pyrenes and the metal center towards the phenanthroline acceptor contribute to the 344-nm absorption band.

Next, the emission spectra of **CuBCP** under excitation at 380-450 nm share similar structureless emission band centered at 580 nm (Figure S8), consistent with its emissive MLCT state. However, the emission bands of **CuPYBCP** varied significantly along with altered excitation wavelengths from 380 to 440 nm (Figure 1c). In detail, a strong emission band peaking at 460 nm can be excited in the range of 380~420 nm, and its intensity was decreased along with the increased excitation wavelength up to 425 nm. Additionally, new emission bands at 550, 653, 720 nm emerged at 395~440 nm excitation, and the strongest emission of these bands was obtained at 425 nm excitation. It is noteworthy that the latter two emission bands are reminiscent of intra-ligand (IL) excited states of some reported pyrene-appended PSs (33, 37-39). Interestingly, the emission intensity at 460 nm sharply decreased with increasing concentration of **CuPYBCP**, while the ones at 550, 653 and 720 nm displayed overall enhancement (Figure S9). The former trend suggests the aggregation-induced quenching with higher concentration of **CuPYBCP**, which should be correlated with the pyrene-involved excited-state species. However, the latter, different tendency infers the presence of another excited state. Moreover, the emission at 460 nm was hardly quenched by air (9%), consistent with singlet emission, whereas the additional emission bands were significantly quenched (over 70%; Figure S10) and should be correlated with triplet species.

We further collected the excitation spectra (Figure 1d) of **CuPYBCP** for the four emission bands. The excitation spectra are identical for emission between 460 and 550 nm, or those between 653 and 720 nm. Notably, an additional band at 420 nm appeared in the excitation spectra responsible for the emission at either 653 or 720 nm, indicating that they should originate from the $MLCT_{phen}$ states in accordance with the TDDFT calculations (Figure 1b). On the other hand, the emission at 460 and 550 nm is attributable the ligand-based excited states, albeit with different relationship vs. [**CuPYBCP**] (Figure S9) and spin states (Figure S10).

More interesting emission behavior was revealed by the measurements of the excited-state lifetimes of **CuPYBCP** (Figure 1e). For the ligand-based emission bands, the monoexponential decay of the emission at 460 nm (excited at 365 nm) is different from the biexponential decay of the one at 550 nm (excited at 425 nm) despite their similarly short lifetimes (3.4 vs. 2.5 ns), further suggesting their different nature. For the $MLCT_{phen}$ emission, the lifetimes of the excited-state species at 653 and 720 nm (both excited at 425 nm) are rather similar (9.4 vs. 9.1 ns) with overlapped decay traces, indicating their same origin. Consequently, three kinds of excited-state species and a dual emission behavior (550 and 653/720 nm) at 425 nm excitation can be revealed from the above observations. Also, it is noteworthy that these lifetime values are dramatically shorter than that of **CuBCP** (289.0 ns), displaying over one-thirtieth shrinkages by appending the pyrene groups. This observation is very unusual since it is contradictory to those pyrene-decorated PSs based on Re (40, 41), Ir (33, 42) and Ru (37, 39) which generally exhibit elongated lifetimes upon the participation of long-lived IL states, highlighting the delicacy of Cu(I) PSs in terms of structural optimizations.

Dual emission behavior is not frequently reported for common PSs, while it could be noticed when inefficient electronic conduction between two distinct emissive excited states in a unified molecule (39). However, it is essential to exclude the factor of a minor impurity inducing the second emissive state. To rule out this possibility, multiple batches of **CuPYBCP** were prepared by three researchers on different scales, all of which afforded identical results within experimental error. Moreover, besides elemental analysis, all batches of **CuPYBCP** were proven to be >99.9% pure by high-performance liquid chromatography. Consequently, to our knowledge, we have eliminated the impurity factor for the observation of dual emission.

In order to address the origins of the dual emission and the rather short excited-state lifetime of **CuPYBCP**, we fully relaxed the low-lying triplet excited states of interest (Table S3-S5). Equilibration of the lowest triplet state from the Franck-Condon geometry by means of DFT (ΔSCF approach) yields a ^{3}MLCT$_{phen}$ state and an emission wavelength of 818 nm (1.52 eV). Accordingly, TDDFT predicts that this ^{3}MLCT$_{phen}$ emission is slightly higher in energy – at 732 nm (1.69 eV). Therefore, the quantum chemical simulations suggest the long wavelength emission observed at 720 nm to be of ^{3}MLCT character. The rather short lifetime of this ^{3}MLCT$_{phen}$ state of merely ~9 ns likely results from the pronounced relativistic effects. On the one hand, the sizeable spin-orbit couplings (SOCs) allow the efficient population transfer to the ^{3}MLCT$_{phen}$ states from the energetically close ^{1}MLCT$_{phen}$ states, i.e., S_1 ^{1}MLCT$_{phen}$ to T_5 and T_9 ^{3}MLCT$_{phen}$ states with SOCs of 119 and 136 cm^{-1}, respectively (Table S3). On the other hand, these relativistic effects also foster a rapid deactivation of the lowest ^{3}MLCT$_{phen}$ to the singlet ground state ($\langle T_1|H_{SOC}|S_0\rangle = 32$ cm^{-1}). The second emission band measured at 653 nm is of similar lifetime (9.4 ns) and stems very likely from a higher lying ^{3}MLCT$_{phen}$ state, such as Franck-Condon states T_5 at 419 nm (2.96 eV) which is initially accessible upon intersystem crossing (ISC) from the dipole-allowed S_1 excitation or from the lower lying T_4 (471 nm, 2.63 eV).

In addition, excited state relaxation channels yielding the population of the two low-lying ^{3}IL$_{pyr}$ states – the locally excited ππ* states – of each pyrene moiety were investigated by means of scalar-relativistic (SR-)TDDFT. Based on the predicted SOCs, these ^{3}IL$_{pyr}$ states are inaccessible from the singlet excited states, as the metal center is not involved in the triplet acceptor states (SOCs of 0~1 cm^{-1}, Table S3). This finding is consistent with previous studies on transition metal complexes combining an inorganic ($^{1/3}$MLCT) and an organic chromophore ($^{1/3}$IL), revealing that an efficient ISC is exclusively observed in scenarios where the metal center is involved in the singlet donor as well as in the triplet acceptor state (43-45). However, the two ^{3}IL$_{pyr}$ states might be accessible upon internal conversion from higher lying ^{3}MLCT$_{phen}$ states. A potential ^{3}IL$_{pyr}$ deactivation is predicted by DFT as well as by TDDFT at merely 1069 and 1072 nm (1.16 eV; ΔSCF) for the two ^{3}IL$_{pyr}$ states, respectively. However, their low energy as well as their inaccessibility by direct ISC suggests that the locally excited states of the pyrene are not involved in the dual emission of **CuPYBCP**. As mentioned above, this finding is at first counterintuitive as Ir (33, 42) and Ru (37, 39) bearing pyrene groups typically feature extended excited-state lifetimes due to the population of long-lived ^{3}IL states which are due to their very small SOCs decoupled to the singlet ground state. However, as we could show in a recent joint synthetic-spectroscopic-theoretical study, such long-lived state is accessible for a related iridium complex due to a pronounced mixing of $^{1/3}$IL states with $^{1/3}$MLCT states (33). This mixed electronic character results in sizeable SOCs up to almost 1000 cm^{-1} and thus fosters the population of the IL state.

Finally, based on the above computational investigations, the emission at 550 nm is unlikely to originate from the monomer form of **CuPYBCP**. Considering its broad, unstructured photoluminescence, as well as its positive concentration dependency (Figure S9) which is opposite to that of the pyrene-based emission band at 460 nm, the emission at 550 nm could be tentatively attributed to the excimer emission (46, 47) of **CuPYBCP**.

Redox properties

Furthermore, cyclic voltammetry with the above spectroscopic results was employed for the estimation of the redox potentials (48, 49) of the Cu(I) PSs (Figure S11), which are also included in Table 1. Potentials are footnoted versus normal hydrogen electrode (vs. NHE) unless otherwise noted. The results firstly indicate that the decoration of pyrenyl groups makes the reversible reduction wave (E_{red} = -1.37 vs. -1.43 V) of **CuPYBCP** less negative to **CuBCP**, suggesting the apparent electron-withdrawing effects of the pyrenyl groups (6, 50). In turn, the reductive quenching potential ($E_{q,red}$ = 1.73 vs. 1.39 V) of **CuPYBCP** is much more positive than that of **CuBCP**. Quantum chemical simulations on the singly reduced doublet species of **CuPYBCP** reveal that the first reduction event is mainly associated to the population of the lowest energy π^*_{phen} orbital (LUMO). However, upon single reduction, this orbital partially extends onto one of the decorating pyrene groups (D_0 in Table S6), which explains the slightly less negative E_{red} with respect to **CuBCP**. Photoexcitation of this doublet species yields several low-lying dipole-allowed doublet transitions of ^{2}ILCT nature – mainly from the π^*_{phen} orbital towards the π^*_{pyr} orbitals (Tables S6, S7 and Figure S12). The above comparison demonstrates a trade-off with pyrene modifications between the two values, both of which serve as the direct or indirect driving forces of reductive quenching pathways for most Cu(I) PSs (22, 27), in which their E_{red} values are already sufficient to drive the catalysis of **CoN5** or **CoPYN5** (ca. -1.1 V) (33).

NMR titration with DFT modeling

^{1}H NMR titration was then applied for evaluations on the binding affinity between **CuPYBCP** and **CoPYN5**, as well as their own self-interaction tendencies. It can be observed that the addition of **CoPYN5** into **CuPYBCP** could induce small shifts of the pyrenyl

protons signals (Figure S13), which were recorded and fitted into several models (see SI and Table S8 for details), in which the non-cooperative 1:2 model was found as the optimal model to afford a 1:1 binding constant (K_{11}) of 207±10 M^{-1}. This value is at the same order of magnitude of the π-π binding constant between a pyrene-dangled Ir(III) PS and **CoPYN5** (199±7 M^{-1}), consistent with the reversible, dynamic nature of the π-π interaction. Moreover, the self-titration experiments of **CoPYN5** (Figure S14) and **CuPYBCP** (Figure S15) reveal dimerization constants of 132±5 and 50±6 M^{-1}, respectively. These above binding behaviors indicate that the hetero-molecular binding can be in a competitive relationship with the self-interactions, but it is still more eminent for its higher binding constant.

With experimental indications, DFT simulations were performed to assess the binding modes as well as the binding energy between **CuPYBCP** and **CoPYN5** in more detail (36). To this aim, π-stacked structures were generated based on the previously sampled conformer space for a related Ir-based PS interacting with **CoPYN5** (33). The DFT-predicted binding energy between the non-reduced **CuPYBCP** (singlet) and the Co(II)-based catalyst (doublet) was calculated to be 0.86 eV (83 kJ mol^{-1}); upon reductive quenching of the excited **CuPYBCP**, the interaction gets stronger with a higher binding energy of 0.92 eV (89 kJ mol^{-1}). These calculations, suggesting a pronounced intermolecular interaction and thus a pre-assembly between **CuPYBCP** and **CoPYN5**, which is in good agreement with previous studies on related π-stacked systems (33, 51, 52). On the other hand, sandwich-like structures, where the pyrene moiety of **CoPYN5** is localized between both pyrene moieties of **CuPYBCP,** were investigated computationally. In both cases of the non-reduced and singly-reduced **CuPYBCP** interacting with **CoPYN5**, their binding energies are almost doubled (non-reduced: 1.37 eV, 132 kJ mol^{-1}; singly reduced: 1.82 eV; 176 kJ mol^{-1}). Furthermore, these sandwich-like structures are also thermodynamically more stable than those stemming from the interactions among only two pyrene moieties (Table S9). However, these sandwiched structures spontaneously feature a singly reduced **CoPYN5** after structural optimization, presumably due to the electron delocalization from the two closely stacked pyrenes (see detailed discussion in SI). Therefore, such sandwiched structures should not be involved in the initial preassembly between the (reduced) **CuPYBCP** and **CoPYN5** but may be of importance for subsequent catalytic cycles and in the underlying electron transfer processes of these later cycles. More details with respect to the binding modes, relative energies and bonding energies are presented in the SI (Table S9 with uploaded data (36)).

Photocatalytic CO_2 reduction

Noble-metal-free systems by pair-wise combinations of the two Cu(I) PSs and the two Co(II) catalysts were evaluated for visible-light-driven CO_2 reduction in a CH_3CN solution containing BIH (1,3-dimethyl-2-phenyl-2,3-dihydro-1H-benzo[*d*]imidazole) as the sacrificial electron donor, triethylamine (TEA) mainly as the deprotonation agent for the oxidized BIH (53), 2,2,2-trifluoroethanol as the proton source and the **xantphos** ligand to suppress the dissociation of Cu(I) PSs (54, 55) during photocatalysis. We note that our previous studies (33, 50) indicate that 2,2,2-trifluoroethanol is the optimal proton source for the Co(II) macrocyclic catalysts over TEA, phenol or water. CO and H_2 were detected as the main products and all the above components are needed to achieve the maximum CO formation (Table S10). The $^{13}CO_2$-labelled reaction generated significant ^{13}CO (*m*/*z* = 29; Figure S16), proving that the source of CO is CO_2 rather than the decomposed organic components.

Table 2. Results of photocatalytic CO_2 reduction experiments.[a]

Entry	PS	Catalyst	*n*(CO) (μmol)	*n*(H_2) (μmol)	TON(CO)[b]	TOF_{1h}(CO)[c] (h^{-1})	TOF_{1h}(H_2)[c] (h^{-1})	CO%	Φ_{1h}
1	**CuBCP**	**CoN5**	35.2±4.6	7.1±2.4	84.5±11.4	84.5±11.4	11.8±5.5	88	6.0%
2	**CuBCP**	**CoPYN5**	71.2±8.2	7.7±2.3	178.0±20.6	178.0±20.6	19.3±5.8	90	12%
3	**CuPYBCP**	**CoN5**	10.2±1.0	3.4±0.8	25.4±2.5	25.4±2.5	8.6±2.0	75	1.8%
4	**CuPYBCP**	**CoPYN5**	135.2±17.4	4.0±1.5	338.0±43.5	263.7±16.1	13.6±3.7	97	19%
5	**RuBPY**	**CoPYN5**	1.8±0.6	0.6±0.1	4.5±1.5	2.9±1.3	1.3±0.2	76	0.3%
6	**IrPPY**	**CoPYN5**	9.0±1.5	0.8±0.2	22.5±3.9	22.5±3.9	2.0±0.5	92	1.4%

[a] Standard condition: Cu PS (0.10 mM), Co catalyst (0.10 mM), TFE (1.0 M), TEA (1.0 M), and BIH (20 mM) in 4.0 mL CH_3CN under 425-nm LED irradiation (50 mW cm^{-2}). The yields of CO and H_2, *n*(CO) and *n*(H_2), were recorded for the maximum values within 120 min irradiation (Figure S18). The experimental errors represent the standard deviations of three independent measurements.
[b] TON = $n(CO)/n_{catalyst}$, in which $n_{catalyst}$ = 0.1 mM × 4.0 mL = 0.4 μmol.
[c] $TOF_{1h} = n(CO)_{1h} / (n_{catalyst} \cdot 1\ h)$.

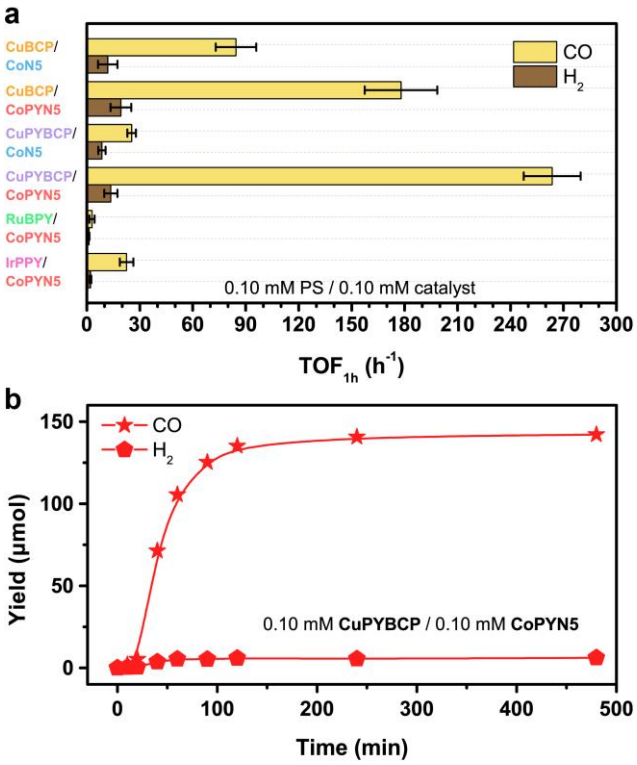

Figure 2. Photocatalytic CO_2 reduction. (a) TOF_{1h} values of CO (yellow) and H_2 (red) yields in the four pairs of Cu(I) PSs (0.10 mM) and Co(II) catalysts (0.10 mM) under 425 nm irradiation for photocatalytic CO_2 reduction. The comparisons with Ru and Ir benchmarking PSs are shown for comparison. Specific conditions and time profiles are shown in Figures S17 and S20. The error bars represent the standard deviations of three independent measurements. (b) Time profiles of photocatalytic CO (star) and H_2 (circle) formation with **CuPYBCP** (0.10 mM), **CoPYN5** (0.10 mM), TFE (1.0 M), TEA (1.0 M), and BIH (20 mM) in 4.0 mL CH_3CN under 425 nm irradiation (50 mW cm^{-2}).

As summarized in Figure S17 and Table 2, the first pair-wise combinations with 0.10 mM catalyst and 0.10 mM PS exhibit the highest TOF_{1h}, TON, selectivity and Φ of the **CuPYBCP**/**CoPYN5** system, suggesting the promotive effect of π-π interaction (Figure 2a). The same activity trend was observed when the catalyst concentration was reduced to 0.01 mM, in which a higher TON of 630±88 was obtained for the most efficient **CuPYBCP**/**CoPYN5** pair (Figure S18 and Table S11). It is interesting to note that the Φ value with **CuBCP** is over three times higher than that with **CuPYBCP** when the pyrene-free **CoN5** acted as the catalyst (6.0% vs. 1.8%), while an inverse order of Φ (12% vs. 19%) was observed with **CoPYN5** instead. These comparisons indicate the relatively unfavorable photo-redox properties of **CuPYBCP** to drive the catalyst with no additional interaction, which, however, have been significantly circumvented by dynamic π-π interaction with **CoPYN5**. The maximum Φ value of 19% at 425 nm during 1 h is higher than our previous π-interacted system with a pyrene-appended Ir(III) PS and **CoPYN5** (14.3 ± 0.8% at 425 nm) (33), which is also higher than most state-of-the-art noble-metal-free systems, including purpurin/[Fe(**qpy**)$(OH_2)_2$](ClO_4) (56) (Φ_{CO} = 1.1% at 450 nm; **qpy** = 2,2′:6′,2″:6″,2‴-quaterpyridine), Cu(II) purpurin/**FeTDHPP** (57) (Φ_{CO} = 6% at 450 nm; **FeTDHPP** = chloroiron(III) 5,10,15,20-tetrakis (2',6'-dihydroxyphenyl)-porphyrin), $[Cu_2(\mathbf{P_2bph})_2]^{2+}$/Fe(**dmp**)$_2(NCS)_2$ (18) (Φ_{CO} = 6.7% at 436 nm; **P$_2$bph** = 4,7-diphenyl-2,9-di(diphenylphosphinotetramethylene)-1,10-phenanthroline; **dmp** = 2,9-dimethyl-1,10-phenanthroline), **CuBCP** with a Mn(I) catalyst (22) (Φ_{CO} = 9.1% at 415 nm), etc. However, it is still lower than the system incorporating $[Cu_2(\mathbf{P_2bph})_2]^{2+}$ and another Mn catalyst (20) ($\Phi_{HCOOH+CO}$ = 57% at 436 nm), which can be mainly attributed to the short-lived excited state of **CuPYBCP**. The main CO production was contributed in the first 2 h of reaction as indicated by a long-term test (Figure 2b). We checked the stability of **CuPYBCP** and **CoPYN5** after the reaction by adding fresh component into the deactivated reaction mixture (Figure S19), where the CO evolution could be largely resumed by the addition of fresh **CoPYN5** instead of **CuPYBCP**, indicating the main deactivated component is the Co(II) catalyst (33). Further delicate screening of PS and catalyst with additional interactions is warranted in our lab for further improvement in catalytic performances.

Additionally, higher activity and selectivity for CO_2 reduction over hydrogen evolution were attained with **CoPYN5** over **CoN5** regardless of the used Cu(I) PS. These differences can be ascribed to our previous finding (33, 50) that the additional pyrene group in **CoPYN5** increased both the redox-activity of the pyridiyldiimine moiety and the hydrophobic nature of the pristine **CoN5** catalyst. It is interesting to note that the photocatalytic evaluations with the use of more concentrated Cu(I) PSs (0.5 mM) display the much-suppressed performances from the systems with **CuPYBCP** (Figure S20 and Table S12), which are even lower than those with **CuBCP** under parallel conditions. These observations should be mainly attributed to the reinforced self-stacking of **CuPYBCP** at high concentrations, as suggested by the NMR self-titration results (Figure S15), which may cause substantial recombination of

photoexcited electrons and holes among the π-π-interacted pyrene-tethered PSs.

We further demonstrated the excellence of this additionally interacted, non-noble-metal system by using noble-metal benchmarking PSs, **RuBPY** (= $[Ru(bpy)_3]Cl_2$, bpy = 2,2'-bipyridine) and **IrPPY** (= *fac*-$Ir(ppy)_3$, ppy = 2-phenylpyridine), in which the Φ value of **CuPYBCP**/**CoPYN5** pair is over 60 and 10 times higher than those of systems with **RuBPY** or **IrPPY** as the PS under identical conditions (19% vs. 0.3%/1.4%; Table 2, Figures 2a and S21), as well as higher CO selectivity (97% vs. 76%/88%), respectively. These intriguing performances which are superior to noble-metal PSs further suggest the merits of additional interactions between PS and catalyst to facilitate the photocatalytic CO_2 reduction.

Overall, the above photocatalytic results demonstrate the promising application of π-π interaction in improving the noble-metal-free systems for photocatalytic CO_2-to-CO conversion.

Photo-induced electron transfer

We then deployed a sequence of fluorescent spectroscopies excited at 425 nm to study the photo-induced electron-transfer pathways and kinetics. The estimated quenching constants via Stern-Volmer plots (see SI for details) are summarized in Table 3. The results of quenching experiments with time-resolved fluorescent spectroscopies indicate that the photoinduced electron transfer follows the reductive quenching pathway (Equation 1-3) in the system with **CuBCP** or **CuPYBCP**. This is because the lifetimes of excited states could be effectively quenched by the addition of BIH rather than the two Co catalysts (see Figures S22-S24). Especially, with BIH addition, much higher dynamic quenching constants were obtained in the case of **CuPYBCP** at 550/653/720-nm emission than the one of **CuBCP** ($1.7\sim2.3 \times 10^{11}$ vs. 8.5×10^9 M^{-1} s^{-1}), approaching to the diffusion limit (58). This tendency is consistent with the much more positive $E_{q,red}$ of **CuPYBCP** than that of **CuBCP** (1.73 vs. 1.39 V).

$$\text{Cu PS} + h\nu \rightarrow \text{Cu PS}^* \quad (1)$$

$$\text{Cu PS}^* + \text{BIH} \xrightarrow{k_{q,red}} \text{Cu PS}^- + \text{BIH}^{\cdot+} \quad (2)$$

$$\text{Cu PS}^- + \text{Co}^{\text{II}}\text{TCPc} \xrightarrow{k_r} \text{Cu PS} + \text{Co}^{\text{I}}\text{TCPc} \quad (3)$$

After forming the reduced state of the Cu(I) PS, the electron of the reduced species will be transferred to the Co(II) catalyst (Equation 3). Therefore, nano-second transient absorption (ns-TA) spectroscopy was utilized to investigate the kinetics of this intermolecular electron-transfer process under the influence of *π-π* interaction. The ns-TA spectra of the reduced Cu(I) PSs could be obtained in the presence of excess BIH and 425 nm excitation. Firstly, for **CuBCP**, excitation induced an excited-state absorption (Figure S25) at 330 and 530 nm, in which the latter can be attributed to the absorption of the ^{3}MLCT species (Figure S8). The excited species has a lifetime (τ_0') of 329 ns, roughly consistent with its fluorescent lifetime τ_0 = 289.0 ns. The addition of an excess of BIH (12 equivalents) induces a long-lived species (τ_1 = 42.6 μs; Figure 3a) with an altered TA spectrum with an absorption at ca. 350 nm, suggesting the generation of the reduced **CuBCP**, which further confirms the reductive quenching pathway. Subsequently, increasing concentration of either **CoN5** or **CoPYN5** could reduce the lifetime of the reduced-state species. The second-order reaction constant (k_r), namely the electron transfer rate from PS to catalyst, for each Co(II) catalyst, can be calculated (32) (Figure 3b-3d, see SI for details and Table 3 for values). The k_r with **CoPYN5** is slightly higher than that with **CoN5** (9.1 vs. 8.7×10^8 M^{-1} s^{-1}; Figure 3h), consistent with the relatively easy reduction of **CoPYN5** to form Co(I) species.

In contrast, the ns-TA spectrum of **CuPYBCP** did not show detectable species due to its short-lived excited state (< 10 ns). Then the addition of excess BIH led to the emergence of a long-lived reduced species (τ_1 = 10.9 μs). The TA temporal evolution of **CuPYBCP** shows a bleaching band at 350 nm and a positive absorption in 400~470 nm range (Figure 3e). According to TDDFT results, this excited-state absorption originates from several dipole and spin-allowed ligand-to-metal and intraligand charge transfer (LMCT and ILCT) transition of the ^{3}MLCT triplet ground state, i.e., into T_{19}, T_{29}, T_{30}, T_{31} and T_{33} (Table S4 and S5). Further addition of each Co(II) catalyst also decreased the longevity of the reduced **CuPYBCP** (Figure 3f and 3g). Notably, the estimated k_r with **CoPYN5** is nearly five times of that with **CoN5** (6.9 vs. 1.4×10^9 M^{-1} s^{-1}; Figure 3h). This is in sharp contrast with the ns-TA results of the **CuBCP** system (Figure 3d and Table 3) in which negligible differences were observed between the two catalysts, which well demonstrates the promotive effect of dynamic *π-π* interaction in accelerating the intermolecular electron transfer process. A very fast PS-to-catalyst electron-transfer rate of 6.9×10^5 s^{-1} (with 0.1 mM catalyst) (32) was achieved, which is faster than the covalently linked Ru(II)-Re(I) dyads ($10^4\sim10^5$ s^{-1}) (59) and a coordinatively interacted Ir(III)-Co(II) combination (2.9×10^5 s^{-1}) (32), but slower than our previous Ir(III)-Co(II) system with *π-π* interaction (2.6×10^6 s^{-1}) (33). We should note that the differences in the utilized transient spectroscopies and the electron-transfer mechanisms should lead to deviations in estimating the electron-transfer kinetics. Overall, the facilitated electron delivery successfully overcomes the negative impact of the very short-lived excited state of **CuPYBCP**, finally achieving a remarkable catalytic efficiency with **CoPYN5** via dynamic *π-π* interaction which is superior to those pyrene-free systems.

Table 3. Related data and calculated rate constants from fluorescent quenching and ns-TA spectroscopy with Cu(I) PSs and Co(II) catalysts.[a]

PS	Time-resolved fluorescent quenching		ns-TA			
	τ_0 (ns)	$k_{q(BIH)}$ (M^{-1} s^{-1})	τ_0' (ns)	τ_1 (μs)	$k_{r(\mathbf{CoN5})}$ ($\times 10^9$ M^{-1} s^{-1})	$k_{r(\mathbf{CoPYN5})}$ ($\times 10^9$ M^{-1} s^{-1})
CuBCP	289.0	8.5×10^9	329.0	42.8	0.87	0.91
CuPYBCP	2.5 (550 nm) 9.4 (653 nm) 9.1 (720 nm)	1.7×10^{11} (550 nm) 2.3×10^{11} (653 nm) 2.0×10^{11} (720 nm)	N.A.	10.9	1.4	6.9

[a] τ_0 and τ_0' are the excited-state lifetimes, $k_{q(BIH)}$ is the reductive quenching constant, τ_1 are the reduced-state lifetimes, $k_{r(\mathbf{CoN5})}$ and $k_{r(\mathbf{CoPYN5})}$ are the second-order reaction constants between the reduced-state PS and the ground-state catalyst.

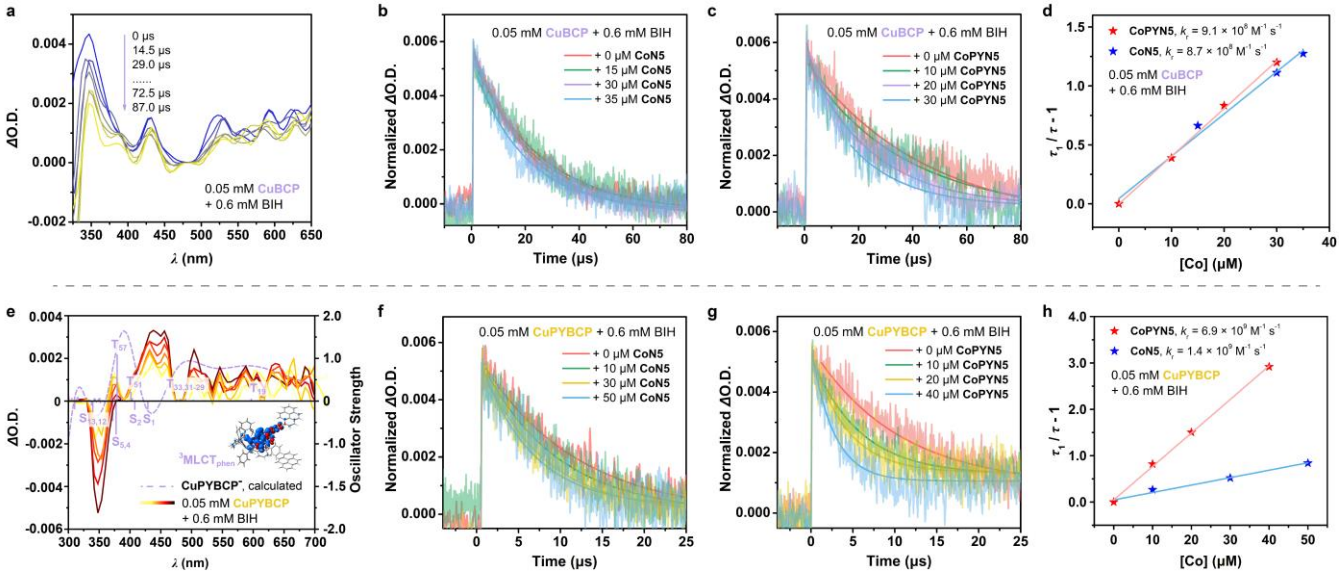

Figure 3. TA experiments. (a) TA spectra of 0.05 mM **CuBCP** with 0.60 mM BIH. Kinetic traces of 0.05 mM **CuBCP** with 0.60 mM BIH and (b) 0~35 μM **CoN5** or (c) 0~30 μM **CoPYN5**. (d) Plot of (τ_1 / τ - 1) versus the concentration of **CoPYN5** (red) or **CoN5** (blue) with linear fitting for the **CuBCP** system with BIH. (e) TA spectra of 0.05 mM **CuPYBCP** with 0.60 mM BIH. The DFT-simulated absorption spectrum (violet, dashed line) and structure (inset) of **CuPYBCP**$^-$ are shown. Kinetic traces of 0.05 mM **CuPYBCP** with 0.60 mM BIH and (f) 0~50 μM **CoN5** or (g) 0~40 μM **CoPYN5**. (h) Plot of (τ_1 / τ - 1) versus the concentration of **CoPYN5** (red) or **CoN5** (blue) with linear fitting for the **CuPYBCP** system with BIH. The kinetic data were collected by following the spectra at 350 nm in Ar-saturated CH_3CN upon excitation at 425 nm.

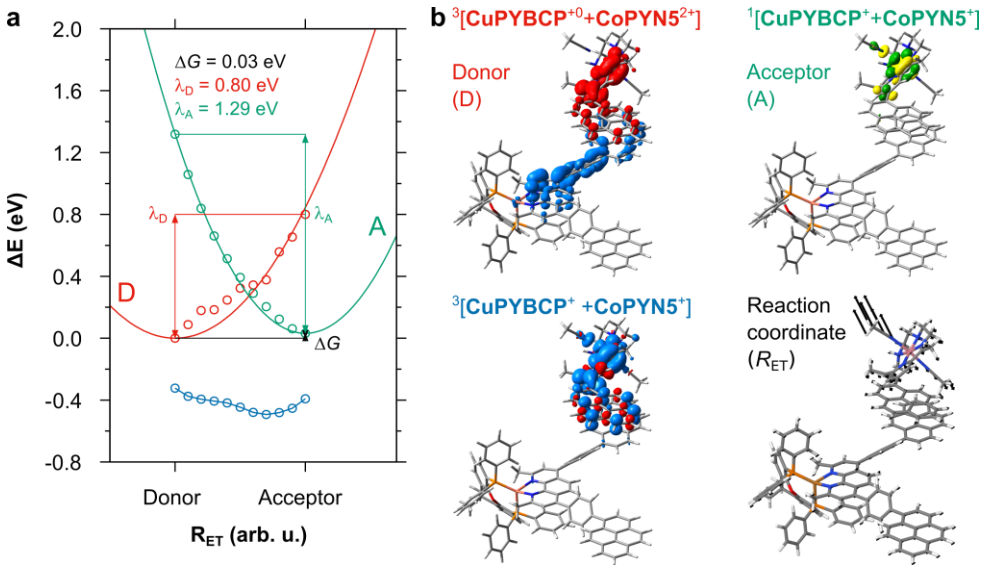

Figure 4. Electron transfer model. (a) Simulated potential energy curves obtained along a linear-interpolated internal reaction coordinate (R_{ET}) connecting (b) the fully optimized ^{3}[**CuPYBCP**$^{+0}$ + **CoPYN5**$^{2+}$] donor state (in red; charge density difference is shown, charge transfer takes place from blue to red) and the ^{3}[**CuPYBCP**$^{+0}$ + **CoPYN5**$^{2+}$] acceptor state (in green; doubly occupied d_{z^2}(Co) acceptor orbital is shown). Quadradic polynomials were fitted to the donor (in red) and acceptor (in blue) states, respectively. Driving force (ΔG) and reorganization energies (λ_D and λ_A) are indicated. A further intermediate is shown in blue, ^{3}[**CuPYBCP**$^+$ + **CoPYN5**$^{2+}$], which features a reduced catalyst with the two unpaired electrons localized in a π_{pyr}* orbital as well in the d_{z^2}(Co), see spin density. The reaction coordinate – associated to dissociation of one solvent molecule from the Co center – is visualized.

To investigate the intermolecular electron-transfer processes between the PS (**CuPYBCP**) and the Co(II) catalyst (**CoPYN5**) in more detail, quantum chemical simulations were performed to assess the associated thermodynamic properties, *i.e.*, driving forces (ΔG), reorganization energies (λ), the underlying reaction coordinate as well as the nature of the involved (photo)redox intermediates. We focused our computational studies exclusively on the reductive quenching pathway (Equation 1-3), as experimentally suggested by the Stern-Volmer kinetics. To this aim, the previously discussed (non-sandwich-like) dimer structure, combining the singly reduced PS and the non-reduced catalyst (Table S9), was used as electron donor state (D in Figure 4). The respective Co(I) intermediate with a doubly occupied d_{z^2}(CO) orbital was considered as electron acceptor state. Noteworthy and due to computational reasons, the donor state was investigated within triplet multiplicity (open-shell), while the acceptor state was evaluated as (closed-shell) singlet state at the density and the time-dependent density levels of theory (DFT and TDDFT). A linear-interpolated reaction coordinate (R_{ET}) was constructed that connects the fully equilibrated structures of the donor and the acceptor state.(36) The respective diabatic potential energy curves of the electron donor state as well as of the electron acceptor state are visualized in Figure 4a, while the underlying reaction coordinate is shown in Figure 4b. The most prominent structural rearrangement along R_{ET} is associated to the formation of the Co(I) species with a stable d^8 configuration, which leads in consequence to a lowered coordination number and the dissociation of CH_3CN molecule (solvent), reminiscent of the computational studies on **CoN5** for CO_2 reduction (60). Based on the energies of the two diabatic states of interest in their respective equilibria, a driving force of merely 0.03 eV (ΔG) and reorganization energies of 0.80 (λ_D) and 1.29 eV(λ_A) were obtained. Unfortunately, the rate constants for such electron-transfer process within the semi-classical Marcus picture, as previously done for light-driven electron-transfer processes in photocatalytic dyads (61-63) could not be calculated due to the approximated spin states of the donor (triplet) and the acceptor (singlet) states. However, the weak driving force suggests a rather slow rate and the formation of an equilibrium. Therefore, the initial computational results present a clear contradiction to the rapid electron transfer observed for the **CuPYBCP/CoPYN5** couple.

Nevertheless, a closer look at further available electron-transfer states yields an alternative energetically low-lying acceptor state, where the electron is not transferred from the π^*_{pyr} of the reduced PS into the d_{z^2}(Co)-orbital to form the Co(I) species, but into the respective low-lying π^*_{pyr} of the pyrene moiety of **CoPYN5** (Figure 4b, in blue). This process also yields a singly reduced catalyst, while it is an open-shell intermediate which is in all investigated structures energetically well below the Co(I) closed-shell species and also thermodynamically more favorable than the donor state. Consequently, the population of such alternative acceptor state with the electron being transferred to the pyrenyl π-system of **CoPYN5** shows a stronger driving force of at least -0.49 eV (Figure 4a) as predicted along R_{ET}. In contrast, such species are not available in **CoN5** due to the absence of the pyrene group. Eventually, the combined experimental and computational results suggest the population of different electron-acceptor states in **CoPYN5** and **CoN5** accounts for the sharply varied electron-transfer rates, which include a rather inefficient and slow population of the d_{z^2}(Co) orbital (1.4×10^9 M^{-1} s^{-1}; Figure 3h) which is available for both catalysts, and a more efficient and faster (6.9×10^9 M^{-1} s^{-1}; Figure 3h) population that generates the open-shell species only in **CoPYN5** based on its highly accessible low-lying π^* orbital.

Proposed mechanism

With the confirmed reductive quenching pathway, and our previous investigations on the catalytic mechanism of **CoPYN5** (33, 50) an overall photocatalytic cycle can be proposed for the **CuPYBCP/CoPYN5** system in CO_2 reduction in Figure 5. The excited state of **CuPYBCP** will react with BIH via the reductive quenching pathway to generate its reduced state. Then the electron can be facilely transferred from the reduced-state species to **CoPYN5** through π-π interaction. Notably, the π-system of the pyrene is

not only involved in the preassembly of the PS and the catalyst, but also acts – according to the performed (TD)DFT simulations – as the potential electron acceptor of **CoPYN5**. The two electron-transfer processes discussed above have been experimentally identified by spectroscopic analyses and theoretical modelling. Next, in the cycle of **CoPYN5** catalyst, its binding with CO_2 requires the second one-electron reduction, possibly by another reduced-state species of **CuPYBCP** (Figure 5), or by the strongly reducing BI· radical (53) from the deprotonated $BIH^{\cdot+}$. CO_2 will bind to the doubly reduced Co catalysts. The C atom of CO_2 will coordinate to the Co center of the doubly reduced **CoPYN5**, which induces a bending of CO_2 due to its partial reduction by the catalyst and population of one π^*_{CO} orbital (50, 60). The Co-CO_2 adduct will be protonated by the proton source and undergo C-OH cleavage to afford Co-carbonyl species, which releases CO and recovers the catalyst.

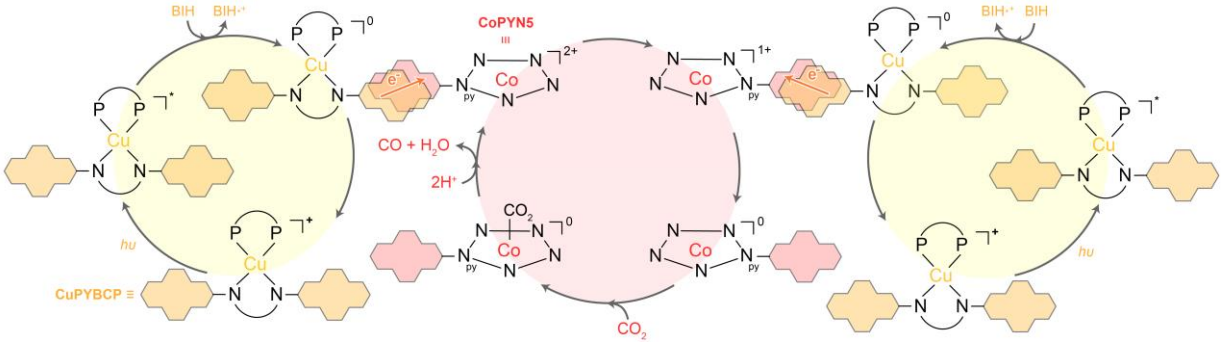

Figure 5. Mechanism. Proposed photocatalytic mechanism for the reduction of CO_2 using the **CuPYBCP/CoPYN5** system.

Conclusion

Heteroleptic Cu(I) complexes have been extensively deployed in the noble-metal-free systems for photocatalytic CO_2 reduction, while the further elevation of their catalytic performances presents challenging. The elegant design of ligand scaffold should allow the creation of Cu(I) PSs with novel photophysical properties for promoting the photocatalysis. After screening out excellent PSs and catalysts upon ligand engineering, a more fundamental strategy can be the installation of additional interactions between them, aiming at a boosted intermolecular electron transfer to facilitate the formation of catalytically active species. In this work, we expanded the library of Cu(I) PSs for CO_2 photoreduction with a rare dual-emissive Cu(I) complex derived from pyrene decorations on the diimine ligand. Compared to its pyrene-free prototype, **CuPYBCP** exhibits unusual photophysical properties besides the dual emission, including the much stronger visible-light absorption (Figure 1b), the excitation-dependent emission behavior (Figure 1c) and the over 30 times more short-lived excited states (ca. 9 vs. 289 ns, Figure 1d). With experimental and computational proofs, under excitation at 425 nm, the emission at 653 and 720 nm can be rationalized as an ^{3}MLCT excited state and the other one at 550 nm can be tentatively attributed to an excimer emission.

More impressively, as a proof-of-concept based on fully earth-abundant elements, the cooperation between **CuPYBCP** and the pyrene-appended **CoPYN5** catalyst successfully established a noble-metal-free system for visible-light-driven CO_2 reduction possessing π-π interactions between PS and catalyst. As demonstrated by NMR titration (Figure S13), DFT simulations (Table S9 and Figure 4) and ns-TA spectroscopies (Figure 3), the dynamic π-π interaction plays a key role in expediting the electron transfer from the reduced Cu(I) PS to the pyrene-appended catalyst, circumventing the unfavorable photocatalytic capabilities of **CuPYBCP**. Consequently, a remarkable Φ of 19% at 425 nm can be accomplished for selective CO_2-to-CO conversion, substantially outperforming the parent **CuBCP** and two noble-metal-based PSs under parallel conditions. Compared to our previously work on a π-π interacted Ir(III)-Co(II) system (33), the next-generation Cu(I)-Co(II) is highly advantageous in the absence of precious metals, the higher catalytic performance (Φ = 19% vs. 14%) and a clearer mechanism for the accelerated

electron transfer demonstrated by quantum chemical calculations. Based on the above interesting results, we believe that our work opens a new avenue to the exploitation and investigations of efficient earth-abundant systems for CO_2 photoreduction and offer valuable insights for the delicate synthetic modifications on the photophysics of Cu(I) PSs.

Methods

Materials

CuBCP (64), BIH (65), **CoN5** (66) and **CoPYN5** (50) were prepared following the previously reported methods and other chemicals were commercially available and used without further purification. *Caution! Perchlorate salts of metal complexes with organic ligands are potentially explosive and should be handled in small quantities with care.*

Synthesis of pybcp ligand

The pyrene-decorated ligand was prepared via Suzuki coupling reaction. 1 mmol 4,7-dibromo-2,9-dimethyl-1,10-phenanthroline, 2.5 mmol of (4-pyrenylphenyl)boronic acid, 15 mol% $P(PPh_3)_4$ and 3 mmol K_2CO_3 were dissolved in 50 mL THF/H_2O (v:v = 5:1) and degassed with argon. After refluxing for 1 day, the reaction mixture was cooled to room temperature and subjected to extraction with DCM, followed by washing with brine twice and then drying over $MgSO_4$. The column chromatography with DCM/CH_3OH (2%) afforded the yellow powder with 52% yield. Elemental Analysis ($C_{58}H_{36}N_2$): Calculated: C, 91.55; H, 4.77; N, 3.68; Measured: C, 91.46; H, 4.84; N, 3.62. ^{1}H NMR (400 MHz, $CDCl_3$) δ 8.34 – 8.18 (m, 12H), 8.17 – 8.00 (m, 18H), 7.88 – 7.74 (m, 11H), 7.73 – 7.62 (m, 5H), 7.60 – 7.42 (m, 4H), 3.11 (s, 6H). ESI-MS(+): [**pybcp**+H]$^+$ (*m*/*z* = 761.3).

Synthesis of CuBCP/CuPYBCP

The synthesis follows a similar procedure for preparing heteroleptic Cu(I) PSs (16). In a 50 mL Schlenk tube, $[Cu(CH_3CN)_4]PF_6$ (186 mg, 0.5 mmol) and xantphos (279 mg, 0.5 mmol) or xantphos (289 mg, 0.5 mmol) are dissolved in 10 mL dry DCM at room temperature under N_2 and darkness. The resulting solution is stirred at 40 °C for 2 h. The reaction mixture was then slowly added with the **bcp**/**pybcp** ligand (0.5 mmol) under N_2 flow. The resulting mixture is then heated at 45 °C for 2 h. The reaction mixture was then cooled to room temperature and underwent precipitation by pouring into 200 mL dry hexane, giving **CuBCP**/**CuPYBCP** as bright yellow powder (86%/75% yield). For **CuPYBCP**, elemental analysis ($CuC_{97}H_{68}N_2OP_3F_6$): Calculated: C, 75.26; H, 4.43; N, 1.81; Measured: C, 74.99; H, 4.53; N, 1.72. ^{1}H NMR (4.0 mM, 400 MHz, CD_3CN) δ 8.37 – 8.17 (m, 13H), 8.16 – 8.02 (m, 6H), 7.93 (s, 2H), 7.85 – 7.76 (m, 6H), 7.71 – 7.66 (m, 4H), 7.59 (s, 2H), 7.31 (dt, *J* = 18.1, 7.9 Hz, 7H), 7.24 – 7.16 (m, 8H), 7.16 – 7.05 (m, 11H), 2.33 (s, 6H), 1.75 (s, 6H). ^{13}C NMR (126 MHz, CD_3CN) δ 158.11, 154.86, 149.29, 143.56, 141.76, 136.44, 135.59, 133.91, 133.44, 133.02, 132.96, 132.90, 131.65, 131.52, 131.44, 131.40, 130.88, 130.84, 130.21, 130.01, 129.73, 128.65, 128.61, 128.58, 128.21, 127.95, 127.84, 127.71, 127.65, 127.38, 126.47, 125.62, 125.52, 125.39, 125.13, 124.94, 124.70, 124.61, 124.49, 123.29, 121.66, 121.56, 121.46, 35.94, 27.90, 26.90. ^{31}P NMR (202 MHz, CD_3CN) δ -9.90. Q-TOF HR-ESI-MS(+): [Cu(**xantphos**)(**pybcp**)]$^+$ (measured: 1401.4065; simulated: 1401.4097). FT-IR (cm^{-1}): 3049 (w), 2925 (w), 1603 (w), 1577 (w), 1481 (w), 1434 (m), 1403 (s), 1224 (m), 1095 (w), 1025 (w), 1003 (w), 834 (s), 742 (m), 722(m), 693 (m), 556 (m), 512 (m).

Data availability

Experimental details, Supplementary figures and tables, and computational data are available from the authors. Most data generated in this study are provided in the Supporting Information/Source Data file. Source data are provided with this paper.

Acknowledgements

We are grateful for the transient absorption spectroscopy operated by Xiao-Liang Ma from Institute for New Energy Materials and Low Carbon Technologies in Tianjin University of Technology, as well as the luminescence analysis supported by Ms. Yu-Xin Chen and Ms. Min-Qi Chen from the Instrumental Analysis and Research Center in Sun Yat-sen University. Gangfeng Ouyang thanks the National Natural Science Foundation of China (21737006, 22076222 and 22036003). Jia-Wei Wang acknowledges the financial supports from Guangdong Basic and Applied Basic Research Foundation (2020A1515110017 and 2021A1515012033). Quantum chemical calculations were performed at the Universitätsrechenzentrum of the Friedrich Schiller University Jena.

Author contributions

J.W.W. conceived this project and organized the collaborations, J.W.W. synthesized the metal complexes, J.W.W., Z.L., Z.M.L. and Y.H. performed the photocatalytic experiments, J.W.W. and Z.L. carried out the fluorescence spectroscopies, S.K carried out the (TD)DFT calculation, J.W.W., S.K. and O.G. analyzed the bulk data and provided the funding. J.W.W. and S.K. co-wrote the main draft of the manuscript. The manuscript was written through contributions of all authors. All authors have given approval to the final version of the manuscript.

References

1. K. E. Dalle*, et al.* Electro- and Solar-Driven Fuel Synthesis with First Row Transition Metal Complexes. *Chem. Rev.* **119**, 2752-2875 (2019).
2. Y. Yamazaki, M. Miyaji, O. Ishitani. Utilization of Low-Concentration CO_2 with Molecular Catalysts Assisted by CO_2-Capturing Ability of Catalysts, Additives, or Reaction Media. *J. Am. Chem. Soc.* **144**, 6640-6660 (2022).
3. N. W. Kinzel, C. Werle, W. Leitner. Transition Metal Complexes as Catalysts for the Electroconversion of CO_2: An Organometallic Perspective. *Angew. Chem. Int. Ed.* **60**, 11628-11686 (2021).
4. E. Boutin, M. Robert. Molecular Electrochemical Reduction of CO_2 beyond Two Electrons. *Trends Chem.* **3**, 359-372 (2021).
5. J.-W. Wang, W.-J. Liu, D.-C. Zhong, T.-B. Lu. Nickel complexes as molecular catalysts for water splitting and CO_2 reduction. *Coord. Chem. Rev.* **378**, 237-261 (2019).
6. Y. Huang*, et al.* Impaired conjugation boosts CO_2 electroreduction by Ni(II) macrocyclic catalysts immobilized on carbon nanotubes. *J. Mater. Chem. A*, in press, 10.1039/d2ta08781b, (2023).
7. J.-W. Wang*, et al.* Facile electron delivery from graphene template to ultrathin metal-organic layers for boosting CO_2 photoreduction. *Nat. Commun.* **12**, 813 (2021).
8. L. Q. Qiu*, et al.* Prolonging the Triplet State Lifetimes of Rhenium Complexes with Imidazole-Pyridine Framework for Efficient CO_2 Photoreduction. *Chem. - Eur. J.* **27**, 15536-15544 (2021).
9. K. M. Van Allsburg*, et al.* Early-stage evaluation of catalyst manufacturing cost and environmental impact using CatCost. *Nat. Catal.* **5**, 342-353 (2022).
10. H. H. Huang*, et al.* Dual electronic effects achieving a high-performance Ni(II) pincer catalyst for CO_2 photoreduction in a noble-metal-free system. *Proc. Natl. Acad. Sci. U. S. A.* **119**, e2119267119 (2022).
11. Y. Kuramochi, R. Sato, H. Sakuma, A. Satake. Photocatalytic CO_2 reduction sensitized by a special-pair mimic porphyrin connected with a rhenium(I) tricarbonyl complex. *Chem. Sci.* **13**, 9861-9879 (2022).
12. F. Sueyoshi, X. Zhang, K. Yamauchi, K. Sakai. Controlling the Photofunctionality of a Polyanionic Heteroleptic Copper(I) Photosensitizer Using Its Ion-pair Formation with Polycationic Ammonium in Aqueous Media. *Angew. Chem. Int. Ed.*, in press, 10.1002/anie.202217807, (2023).
13. J. W. Wang*, et al.* Homoleptic Al(III) Photosensitizers for Durable CO_2 Photoreduction. *J. Am. Chem. Soc.* **145**, 676-688 (2023).
14. Y. Zhang*, et al.* Heteroleptic diimine–diphosphine Cu(I) complexes as an alternative towards noble-metal based photosensitizers: Design strategies, photophysical properties and perspective applications. *Coord. Chem. Rev.* **356**, 127-146 (2018).
15. A. Hossain, A. Bhattacharyya, O. Reiser. Copper's rapid ascent in visible-light photoredox catalysis. *Science* **364**, eaav9713 (2019).
16. S. P. Luo*, et al.* Photocatalytic water reduction with copper-based photosensitizers: a noble-metal-free system. *Angew. Chem. Int. Ed.* **52**, 419-423 (2013).
17. P. A. Forero Cortés, M. Marx, M. Trose, M. Beller. Heteroleptic copper complexes with nitrogen and phosphorus ligands in photocatalysis: Overview and perspectives. *Chem Catal.* **1**, 298-338 (2021).
18. H. Takeda, K. Ohashi, A. Sekine, O. Ishitani. Photocatalytic CO_2 Reduction Using Cu(I) Photosensitizers with a Fe(II) Catalyst. *J. Am. Chem. Soc.* **138**, 4354-4357 (2016).
19. H. Takeda, Y. Monma, O. Ishitani. Highly Functional Dinuclear Cu^{I}-Complex Photosensitizers for Photocatalytic CO_2 Reduction. *ACS Catal.* **11**, 11973-11984 (2021).
20. H. Takeda*, et al.* Highly Efficient and Robust Photocatalytic Systems for CO_2 Reduction Consisting of a Cu(I) Photosensitizer and Mn(I) Catalysts. *J. Am. Chem. Soc.* **140**, 17241-17254 (2018).
21. A. Rosas-Hernández, C. Steinlechner, H. Junge, M. Beller. Earth-abundant photocatalytic systems for the visible-light-driven reduction of CO_2 to

CO. *Green Chem.* **19**, 2356-2360 (2017).

22. C. Steinlechner, *et al.* Selective Earth-Abundant System for CO_2 Reduction: Comparing Photo- and Electrocatalytic Processes. *ACS Catal.* **9**, 2091-2100 (2019).
23. X. Zhang, K. Yamauchi, K. Sakai. Earth-Abundant Photocatalytic CO_2 Reduction by Multielectron Chargeable Cobalt Porphyrin Catalysts: High CO/H_2 Selectivity in Water Based on Phase Mismatch in Frontier MO Association. *ACS Catal.* **11**, 10436-10449 (2021).
24. X. Zhang, *et al.* Photochemical CO_2 Reduction Driven by Water-Soluble Copper(I) Photosensitizer with the Catalysis Accelerated by Multi-Electron Chargeable Cobalt Porphyrin. *ACS Catal.* **9**, 11263-11273 (2019).
25. R. Hamze, *et al.* Eliminating nonradiative decay in Cu(I) emitters: >99% quantum efficiency and microsecond lifetime. *Science* **363**, 601-606 (2019).
26. J. Li, *et al.* Two-Coordinate Copper(I)/NHC Complexes: Dual Emission Properties and Ultralong Room-Temperature Phosphorescence. *Angew. Chem. Int. Ed.* **59**, 8210-8217 (2020).
27. S. Fischer, *et al.* Death and Rebirth: Photocatalytic Hydrogen Production by a Self-Organizing Copper–Iron System. *ACS Catal.* **4**, 1845-1849 (2014).
28. A. Nakada, K. Koike, K. Maeda, O. Ishitani. Highly efficient visible-light-driven CO_2 reduction to CO using a Ru(II)–Re(I) supramolecular photocatalyst in an aqueous solution. *Green Chem.* **18**, 139-143 (2016).
29. Y. Kuramochi, Y. Fujisawa, A. Satake. Photocatalytic CO_2 Reduction Mediated by Electron Transfer via the Excited Triplet State of Zn(II) Porphyrin. *J. Am. Chem. Soc.* **142**, 705-709 (2020).
30. C. D. Windle, *et al*. Comparison of rhenium-porphyrin dyads for CO_2 photoreduction: photocatalytic studies and charge separation dynamics studied by time-resolved IR spectroscopy. *Chem. Sci.* **6**, 6847-6864 (2015).
31. P. L. Cheung, *et al.* Improving Photocatalysis for the Reduction of CO_2 through Non-covalent Supramolecular Assembly. *J. Am. Chem. Soc.* **141**, 14961-14965 (2019).
32. J. W. Wang, *et al.* Rapid electron transfer via dynamic coordinative interaction boosts quantum efficiency for photocatalytic CO_2 reduction. *Nat. Commun.* **12**, 4276 (2021).
33. J. W. Wang, *et al.* Co-facial π−π Interaction Expedites Sensitizer-to-Catalyst Electron Transfer for High-Performance CO_2 Photoreduction. *JACS Au* **2**, 1359-1374 (2022).
34. H. Nasrallah, P. Lyu, G. Maurin, M. El-Roz. Highly efficient CO_2 reduction under visible-light on non-covalent Ru···Re assembled photocatalyst: Evidence on the electron transfer mechanism. *J. Catal.* **404**, 46-55 (2021).
35. M. Heberle, *et al.* Heteroleptic Copper Photosensitizers: Why an Extended pi-System Does Not Automatically Lead to Enhanced Hydrogen Production. *Chem. - Eur. J.* **23**, 312-319 (2017).
36. S. Kupfer. DFT-predicted equilibrium structures and electron transfer coordinate: CuPYBCP, CoPYN5, and CuPYBCP-CoPYN5. DOI: doi.org/10.5281/zenodo.7260662 (2022).
37. S. Guo, *et al.* Robust and Long-Lived Excited State Ru(II) Polyimine Photosensitizers Boost Hydrogen Production. *ACS Catal.* **8**, 8659-8670 (2018).
38. A. J. Howarth, *et al.* Tuning the emission lifetime in bis-cyclometalated iridium(III) complexes bearing iminopyrene ligands. *Inorg. Chem.* **53**, 11882-11889 (2014).
39. R. Lincoln, *et al.* Exploitation of long-lived ^{3}IL excited states for metal-organic photodynamic therapy: verification in a metastatic melanoma model. *J. Am. Chem. Soc.* **135**, 17161-17175 (2013).
40. M. D. Zott, V. M. Canestraight, J. C. Peters. Mechanism of a Luminescent Dicopper System That Facilitates Electrophotochemical Coupling of Benzyl Chlorides via a Strongly Reducing Excited State. *ACS Catal.* **12**, 10781-10786 (2022).
41. L.-Q. Qiu, K.-H. Chen, Z.-W. Yang, L.-N. He. A rhenium catalyst with bifunctional pyrene groups boosts natural light-driven CO_2 reduction. *Green Chem.* **22**, 8614-8622 (2020).
42. S. K. Seth, P. Purkayastha. Unusually Large Singlet Oxygen ($^1O_2$) Production by Very Weakly Emissive Pyrene-Functionalized Iridium(III) Complex: Interplay between Excited ^{3}ILCT/^{3}IL and ^{3}MLCT States. *Eur. J. Inorg. Chem.* **2020**, 2990-2997 (2020).
43. G. E. Shillito, *et al.* Excited-State Switching Frustrates the Tuning of Properties in Triphenylamine-Donor-Ligand Rhenium(I) and Platinum(II) Complexes. *Inorg. Chem.* **59**, 6736-6746 (2020).
44. G. E. Shillito, *et al.* Dramatic Alteration of ^{3}ILCT Lifetimes Using Ancillary Ligands in $[Re(L)(CO)_3(phen\text{-}TPA)](n+)$ Complexes: An Integrated

Spectroscopic and Theoretical Study. *J. Am. Chem. Soc.* **140**, 4534-4542 (2018).

45. J. J. Sutton, *et al.* Excited-State Switching in Rhenium(I) Bipyridyl Complexes with Donor-Donor and Donor-Acceptor Substituents. *J. Am. Chem. Soc.* **143**, 9082-9093 (2021).
46. M. A. Omary, H. H. Patterson. Luminescence, Theory. In: *Encyclopedia of Spectroscopy and Spectrometry (Third Edition)* (ed^(eds Lindon JC, Tranter GE, Koppenaal DW). Academic Press (2017).
47. S. H. Lee, *et al.* Fluorescence ratiometry of monomer/excimer emissions in a space-through PET system. *J. Org. Chem.* **70**, 9288-9295 (2005).
48. C. B. Larsen, O. S. Wenger. Photoredox Catalysis with Metal Complexes Made from Earth-Abundant Elements. *Chem. - Eur. J.* **24**, 2039-2058 (2018).
49. N. Armaroli. Photoactive mono- and polynuclear Cu(I)–phenanthrolines. A viable alternative to Ru(II)–polypyridines? *Chem. Soc. Rev.* **30**, 113-124 (2001).
50. J.-W. Wang, *et al.* CH-π interaction boosts photocatalytic CO_2 reduction activity of a molecular cobalt catalyst anchored on carbon nitride. *Cell Rep. Phys. Sci.* **2**, 100681 (2021).
51. J. F. Lefebvre, *et al.* An artificial photosynthetic system for photoaccumulation of two electrons on a fused dipyridophenazine (dppz)-pyridoquinolinone ligand. *Chem. Sci.* **9**, 4152-4159 (2018).
52. J. F. Lefebvre, *et al.* Synthesis of three series of ruthenium tris-diimine complexes containing acridine-based pi-extended ligands using an efficient "chemistry on the complex" approach. *Dalton. Trans.* **45**, 16298-16308 (2016).
53. Y. Tamaki, K. Koike, T. Morimoto, O. Ishitani. Substantial improvement in the efficiency and durability of a photocatalyst for carbon dioxide reduction using a benzoimidazole derivative as an electron donor. *J. Catal.* **304**, 22-28 (2013).
54. D. Moonshiram, *et al.* Elucidating the Nature of the Excited State of a Heteroleptic Copper Photosensitizer by using Time-Resolved X-ray Absorption Spectroscopy. *Chem. - Eur. J.* **24**, 6464-6472 (2018).
55. A. Kaeser, *et al.* Heteroleptic copper(I) complexes prepared from phenanthroline and bis-phosphine ligands. *Inorg. Chem.* **52**, 12140-12151 (2013).
56. Z. Guo, *et al.* Highly Efficient and Selective Photocatalytic CO_2 Reduction by Iron and Cobalt Quaterpyridine Complexes. *J. Am. Chem. Soc.* **138**, 9413-9416 (2016).
57. H. Yuan, *et al.* Promoting photocatalytic CO_2 reduction with a molecular copper purpurin chromophore. *Nat. Commun.* **12**, 1835 (2021).
58. A. Rosspeintner, G. Angulo, E. Vauthey. Bimolecular photoinduced electron transfer beyond the diffusion limit: the Rehm-Weller experiment revisited with femtosecond time resolution. *J. Am. Chem. Soc.* **136**, 2026-2032 (2014).
59. K. Koike, *et al.* Investigation of excited state, reductive quenching, and intramolecular electron transfer of Ru(II)-Re(I) supramolecular photocatalysts for CO_2 reduction using time-resolved IR measurements. *Chem. Sci.* **9**, 2961-2974 (2018).
60. L. Chen, *et al.* Molecular Catalysis of the Electrochemical and Photochemical Reduction of CO_2 with Earth-Abundant Metal Complexes. Selective Production of CO vs HCOOH by Switching of the Metal Center. *J. Am. Chem. Soc.* **137**, 10918-10921 (2015).
61. A. Koch, *et al.* Photochemistry and Electron Transfer Kinetics in a Photocatalyst Model Assessed by Marcus Theory and Quantum Dynamics. *J. Phys. Chem. C* **121**, 16066-16078 (2017).
62. M. Staniszewska, S. Kupfer, J. Guthmuller. Effect of the Catalytic Center on the Electron Transfer Dynamics in Hydrogen-Evolving Ruthenium-Based Photocatalysts Investigated by Theoretical Calculations. *J. Phys. Chem. C* **123**, 16003-16013 (2019).
63. M. Staniszewska, S. Kupfer, J. Guthmuller. Theoretical Investigation of the Electron-Transfer Dynamics and Photodegradation Pathways in a Hydrogen-Evolving Ruthenium-Palladium Photocatalyst. *Chem. - Eur. J.* **24**, 11166-11176 (2018).
64. B. F. DiSalle, S. Bernhard. Orchestrated photocatalytic water reduction using surface-adsorbing iridium photosensitizers. *J. Am. Chem. Soc.* **133**, 11819-11821 (2011).
65. X. Q. Zhu, *et al.* Hydride, hydrogen atom, proton, and electron transfer driving forces of various five-membered heterocyclic organic hydrides and their reaction intermediates in acetonitrile. *J. Am. Chem. Soc.* **130**, 2501-2516 (2008).
66. J.-W. Wang, *et al.* A Molecular Cobalt Hydrogen Evolution Catalyst Showing High Activity and Outstanding Tolerance to CO and O_2. *Angew. Chem. Int. Ed.* **58**, 10923-10927 (2019).